

X-Ray spectral evolution of PSR J2032+4127 during the 2017 periastron passage

PARTHA SARATHI PAL,<sup>1</sup> P. H. T. TAM,<sup>1</sup> Y. CUI,<sup>1</sup> K. L. LI,<sup>2</sup> A. K. H. KONG,<sup>3,4</sup> AND C. GÜNGÖR<sup>5</sup>

<sup>1</sup>*School of Physics & Astronomy, Sun Yat Sen University,  
135 West Xingang Road, Guangzhou, 510275, China*

<sup>2</sup>*Department of Physics, Ulsan National Institute of Science and Technology,  
Ulsan, 44919, Korea*

<sup>3</sup>*Astrophysics, Department of Physics, University of Oxford,  
Keble Road, Oxford OX1 3RH, UK*

<sup>4</sup>*Institute of Astronomy & Department of Physics, National Tsing Hua University,  
Hsinchu 30013, Taiwan*

<sup>5</sup>*Faculty of Engineering and Natural Science, Sabanci University,  
Orhanli - Tuzla, Istanbul, 34956, Turkey*

(Received; Revised; Accepted)

Submitted to ApJ

ABSTRACT

We report X-ray data analysis results obtained from *Chandra*, *XMM-Newton*, *NuSTAR* and *Swift* observations of PSR J2032+4127 taken before, during, and after the periastron on 2017 November 13. We found the first clear evidence of a change in the X-ray spectral index over the passage period, thanks to a broad and sensitive spectral coverage by *XMM-Newton* and *NuSTAR*. We analysed the joint *XMM-Newton* and *NuSTAR* observation epochs with power-law and broken power-law model. We have obtained change in spectral parameters before and after the periastron passage for both models. The spectra get softened after the passage. The evolution of the spectral index and break energy before and after the periastron may indicate a change in the physical state of shock-accelerated electrons.

*Keywords:* X-rays: binaries – pulsars: individual (PSR J2032+4127) – stars: individual (MT 91-213)  
– stars: winds, outflows

1. INTRODUCTION

PSR J2032+4127 is a radio-loud GeV emitting pulsar, discovered by *Fermi Large Area Telescope (Fermi-LAT)* in a blind search of *Fermi-LAT* gamma-ray data (Abdo et al. 2009) and was subsequently detected in radio wavelength with the Green Bank Telescope (GBT; Camilo et al. 2009). It is one of the younger member of its class and has a spin period of 143 ms (Abdo et al. 2013). Several observations revealed a variable spin-down rate in the pulsar which is explained as an effect of Doppler shift due to the pulsar’s motion along the orbit of the binary system with long-period (Lyne et al. 2015). The companion star was identified as a Be star, MT 91-213, which has a mass of around  $15 M_{\odot}$  with a circumstellar variable disk within radius 0.2-0.5 AU (Ho et al. 2017). The pulsar spin-down luminosity( $\dot{E}$ ) was determined to be around  $1.7 \times 10^{35} \text{ erg s}^{-1}$  with a characteristic age of 180 kyr, and the binary system is at a distance of 1.44 kpc in the Cyg OB2 stellar cluster (Gaia Collaboration 2018). Further observations precisely determined the orbital parameters with a binary period of 45-50 years, an eccentricity between 0.94 and 0.99 and a longitude of periastron between  $21^{\circ}$  and  $52^{\circ}$ . According to the best fit of radio timing solution the periastron passage was on 2017 November 13 with an approximate separation between PSR J2032+4127 and MT 91-213 of 1 AU (Ho et al. 2017; Coe et al. 2017).

Close to the periastron, due to the expected interaction between the matter of the stellar wind (or possibly the disk) and the pulsar wind, emission of low energy (radio to X-rays) to high energy (GeV or up to TeV) photons are predicted (Takata et al. 2017; Bednarek et al. 2018). Indeed, this object shows similarity with another  $\gamma$ -ray binary PSR B1259-63/LS 2883 (Chernyakova et al. 2015; Tam et al. 2015; Johnson et al. 2018; Tam et al. 2018). PSR B1259-63 has a spin period of 47.8 ms and orbits around the Be star LS 2883 with a period of 3.4 years in a highly eccentric orbit ( $e \sim 0.87$ ). It shows a spin down luminosity around  $8.3 \times 10^{35} \text{ erg s}^{-1}$ . It is known that PSR B1259-63 converts nearly all of its pulsar spin-down luminosity to GeV emission during parts of its orbit (Caliandro et al. 2015). Several models have been proposed to explain the non-thermal, broadband radiation from PSR B1259-63 as well as the GeV flares. These include synchrotron emission and/or inverse-Compton (IC) up-scattering off stellar photons or disk photons from the companion star by the accelerated electrons in the shock between the PW and stellar wind (Tavani & Arons 1997; Kirk et al. 1999; Dubus 2006; Bogovalov et al. 2008; Khangulyan et al. 2011; Takata et al. 2012), unshocked PW particles (Khangulyan et al. 2012), and Doppler boosting effects (Dubus et al. 2010; Takata et al. 2012). As it is accepted that both systems are similar (Ho et al. 2017; Coe et al. 2019), it is understandable that the origin of X-ray & TeV emission for PSR J2032+4127 should be pulsar spin-down luminosity.

Ho et al. (2017) and Li et al. (2017a) first reported the X-ray brightening from the direction of PSR J2032+4127, consistent with the increased shock emission. Ho et al. (2017) has predicted the timing of the periastron from orbital solution. Li et al. (2017b) has summarized *The Neil Gehrels Swift Observatory (Swift)*, *the Chandra X-ray Observatory (Chandra)*, *The Nuclear Spectroscopic Telescope Array Mission (NuSTAR)* and *The European Space Agency's (ESA) X-ray Multi-Mirror Mission (XMM-Newton)* observations of PSR J2032+4127 up to early 2017 and tried to explain the pre-periastron X-ray behaviors of PSR J2032+4127. In continuation of this work, Li et al. (2018) reported the X-ray modulation using Swift data and  $\gamma$ -ray observations of PSR J2032+4127 over the 2017 periastron. The effect of an asymmetric stellar wind with polar gradient is investigated in Petropoulou et al. (2018). Optical variability around the periastron is monitored and reported by Kolka et al. (2017). The VHE gamma-ray counterpart of the 2017 periastron emission was observed by *Very Energetic Radiation Imaging Telescope Array System (VERITAS)* and *Major Atmospheric Gamma Imaging Cherenkov (MAGIC)* (Abeysekara et al. 2018). TeV spectral analysis data is adopted in this paper for comparison with X-Ray analysis result. Takata et al. (2017) explained the multi-wavelength phenomena in light of the shock scenario and discussed the possible formation of an accretion disk. However, the rather rich broad-band data and the complex X-ray flux variability still lacks a full theoretical understanding.

In this paper, we present the result throughout our analysis of the archival data of *Swift*, *XMM-Newton*, *Chandra* and *NuSTAR* to understand the detailed X-ray evolution through the periastron passage. In particular, we report the first accurate X-ray spectral index and interstellar absorption measurements over the 2017 periastron passage of PSR J2032+4127.

## 2. DATA ANALYSIS

During 2017 periastron PSR J2032+4127 was observed by *Swift*, *XMM-Newton*(P.I: Jules Halpern), *Chandra*(P.I.: Jules Halpern), *NuSTAR*(P.I: Jules Halpern). The observation details is shown in Table. 1.

**Table 1.** Observational data analysed in this paper. First column shows the observation dates. Next column shows the observation epoch w.r.t periastron date (MJD 58070). In third column shows the observing instrument. Fourth column shows observation ID. Fifth column shows the exposure time. Sixth column shows count rate during the observation.

Date (MJD)	Epoch (Days)	Instrument	Obs-Id	Exposure Sec	Rate counts/s
57442.34	-628.16	<i>Chandra</i>	18788	4896	0.03±0.003
57785.20	-285.30	<i>Chandra</i>	19607	26640	0.07±0.002
57901.66	-168.84	<i>Chandra</i>	19700	28160	0.15±0.002
57976.33	-94.17	<i>SWIFT</i>	93146011	3336	0.04±0.003
57987.51	-82.99	<i>SWIFT</i>	34282090	1166	0.04±0.006
57990.10	-80.40	<i>SWIFT</i>	34282091	1992	0.03±0.004
57991.36	-79.14	<i>SWIFT</i>	93146012	2651	0.04±0.004

continued . . .

... continued

Date (MJD)	Epoch (Days)	Instrument	Obs-Id	Exposure Sec	Rate counts/s
57994.08	-76.42	<i>Chandra</i>	19701	28400	0.13±0.002
58002.05	-68.45	<i>SWIFT</i>	93148006	2804	0.04±0.004
58007.22	-63.28	<i>SWIFT</i>	93148007	1146	0.03±0.006
58017.00	-53.50	<i>SWIFT</i>	93148008	2437	0.05±0.004
58018.38	-52.12	<i>SWIFT</i>	34282094	1613	0.06±0.006
58019.91	-50.59	<i>SWIFT</i>	93146014	1455	0.04±0.007
58026.15	-44.35	<i>SWIFT</i>	93146015	2956	0.04±0.004
58032.59	-37.91	<i>SWIFT</i>	93148009	2614	0.05±0.004
58033.32	-37.18	<i>SWIFT</i>	93146016	3221	0.04±0.004
58039.11	-31.39	<i>SWIFT</i>	34282097	1418	0.05±0.006
58039.32	-31.18	<i>SWIFT</i>	93148010	3576	0.05±0.004
58046.09	-24.41	<i>SWIFT</i>	34282098	1988	0.05±0.005
58047.08	-23.42	<i>SWIFT</i>	93146018	2710	0.05±0.005
58047.35	-23.15	<i>SWIFT</i>	93148011	2083	0.03±0.004
58049.48	-21.02	<i>SWIFT</i>	88016001	1756	0.04±0.005
58049.51	-20.99	<i>NuSTAR</i>	30302002002	37843	0.06±0.001
58049.74	-20.76	<i>XMM</i>	801910201	22643	0.43±0.005
58050.74	-19.76	<i>SWIFT</i>	34282099	2894	0.04±0.004
58051.13	-19.37	<i>SWIFT</i>	93148012	1893	0.04±0.005
58053.00	-17.50	<i>SWIFT</i>	34282100	1096	0.04±0.006
58054.92	-15.58	<i>SWIFT</i>	93146019	2789	0.04±0.004
58057.51	-12.99	<i>SWIFT</i>	34282101	1626	0.03±0.005
58060.25	-10.25	<i>Chandra</i>	19702	19080	0.12±0.003
58060.64	-9.86	<i>SWIFT</i>	34282103	1981	0.03±0.004
58061.04	-9.46	<i>SWIFT</i>	93146020	3328	0.03±0.003
58062.20	-8.30	<i>NuSTAR</i>	90302321002	39826	0.03±0.001
58062.76	-7.74	<i>SWIFT</i>	93148013	3219	0.02±0.003
58062.78	-7.72	<i>XMM</i>	801910301	16657	0.22±0.004
58062.89	-7.61	<i>Chandra</i>	20836	9560	0.10±0.003
58065.41	-5.09	<i>SWIFT</i>	34282106	1848	0.02±0.004
58068.14	-2.36	<i>SWIFT</i>	93146021	2349	0.03±0.004
58069.78	-0.72	<i>NuSTAR</i>	30302002004	42705	0.03±0.001
58069.87	-0.63	<i>SWIFT</i>	34282108	1526	0.02±0.004
58070.50	0.00	<i>XMM</i>	801910401	11518	0.21±0.005
58071.85	1.35	<i>SWIFT</i>	34282109	2333	0.01±0.003
58074.65	4.15	<i>SWIFT</i>	34282110	1953	0.03±0.004
58075.58	5.08	<i>SWIFT</i>	93146022	2817	0.02±0.003
58076.10	5.60	<i>SWIFT</i>	34282111	2250	0.02±0.003
58077.50	7.00	<i>SWIFT</i>	93148015	3366	0.04±0.003
58078.51	8.01	<i>NuSTAR</i>	90302321004	40003	0.06±0.001
58078.96	8.46	<i>SWIFT</i>	34282112	1483	0.05±0.006
58079.05	8.55	<i>XMM</i>	801910501	17958	0.49±0.006
58081.35	10.85	<i>SWIFT</i>	34282114	1491	0.04±0.005
58082.21	11.71	<i>SWIFT</i>	93146023	1274	0.04±0.006
58083.14	12.64	<i>SWIFT</i>	34282115	1973	0.04±0.005
58084.14	13.64	<i>SWIFT</i>	93148016	2172	0.05±0.005

continued ...

... continued

Date (MJD)	Epoch (Days)	Instrument	Obs-Id	Exposure Sec	Rate counts/s
58085.00	14.50	<i>SWIFT</i>	34282116	2317	0.05±0.005
58087.21	16.71	<i>SWIFT</i>	34282117	2028	0.04±0.005
58089.13	18.63	<i>SWIFT</i>	93146024	2130	0.05±0.005
58091.46	20.96	<i>NuSTAR</i>	30302002006	41531	0.04±0.001
58091.72	21.22	<i>XMM</i>	801910601	16756	0.36±0.006
58092.73	22.23	<i>SWIFT</i>	93148017	3122	0.04±0.004
58095.38	24.88	<i>SWIFT</i>	34282119	1465	0.02±0.004
58095.44	24.94	<i>SWIFT</i>	10451001	3459	0.00±0.002
58127.99	57.49	<i>Chandra</i>	19608	29030	0.11±0.002
58193.59	123.09	<i>Chandra</i>	19698	29160	0.04±0.001

*XMM-Newton* have observed PSR J2032+4127 on 5 different epochs between MJD 58049 to 58091 with an average 17 ks exposure. *XMM-Newton EPIC-PN* and *MOS* data are used for the X-ray analysis in this paper. The data reduction were reprocessed with the software *SASv16.1*<sup>1</sup>, using the most updated calibration files (updated to 2018 May) (Strüder et al. 2001; Turner et al. 2001). The *EPIC-PN* event files were reprocessed from observation data files with *emproc* with ‘bad’(e.g., ‘hot’, ‘dead’, ‘flickering’) pixels removed. The period of high background events were examined and excluded using the light curves in the energy band 10-12 keV. As the X-ray of PSR J2032+4127 is not bright and there is no pile-up effect, we extracted the source events from a circular region of radius 20'', using single and double events (PATTERN≤4, FLAG=0). The background events were made from a source-free circular region of radius of 20''. We grouped the pn spectra to have at least 25 counts in each bin, so as to adopt the  $\chi^2$  statistic for the spectral fitting. The ancillary response files (arfs) were extracted with *arfgen*. The *EPIC-PN* redistribution matrix file was extracted with *rmfgen* and used in spectral fitting. Similarly *EPIC-MOS* event files were reprocessed from observation data files with *emproc* with ‘bad’(e.g., ‘hot’, ‘dead’, ‘flickering’) pixels removed. The period of high background events were examined and excluded using the light curves in the energy band above 10 keV. We checked for pile-up and the pile-up effect is not serious in the source center. We extracted the source events from a circular region of radius 20'', using single and double events (PATTERN≤12). We grouped the pn spectra to have at least 25 counts in each bin, so as to adopt the  $\chi^2$  statistic for the spectral fitting. The ancillary response files (arfs) were extracted with *arfgen*. We repeated the similar extraction method for *MOS1* and *MOS2* spectra. During fitting we used both of them as different data groups.

*NuSTAR* have observed PSR J2032+4127 almost simultaneously with *XMM-Newton* enabling us to perform a joint spectral analysis for *XMM* and *NuSTAR*. The *NuSTAR* event files are obtained with *nupipeline* of *HEASOFTv6.25*<sup>2</sup> software (Harrison et al. 2013). We have used *SW\_SAA=0* and *SW\_TENTACLE=0* during analysis to avoid background flaring. With *nuproduct* the source spectra are extracted from a circular region of 30'' as the source position and the background is estimated from a source free region of same size. The spectra are grouped with 30 counts per bin for spectral analysis. The response functions and ancillary response files are also extracted. Both *FPMA* and *FPMB* spectra are used for spectral analysis. During fitting we used both *FPMA* and *FPMB* as different data groups.

*Chandra* have observed PSR J2032+4127 on 5 different epochs around 2017 periastron between MJD 57785 and MJD 58062 with average 20 ks exposure. The data reduction is performed with *CIAOv4.9*<sup>3</sup> software (Weisskopf et al. 2000). The fits files are cleaned for high flaring backgrounds. The spectra are extracted from a circular region of 7'' at the source position and background is estimated from a source free region with same radius from the cleaned fits file. We grouped *ACIS* spectra to have at least 15 counts in each bin for spectral analysis. The PI had chosen a smaller good exposure time in the proposal to avoid the pile-up effect. We have tested the spectra with *XSPEC* pile-up model but there is no pile-up effect observed in the spectra.

For *Swift-XRT* data reduction, the level 2 cleaned event files of *Swift-XRT* are obtained from the events of photon counting (PC) mode data with *xrtpipeline* (Burrows et al. 2005). The spectra are extracted from a circular region

<sup>1</sup> <https://www.cosmos.esa.int/web/xmm-newton/sas-threads>

<sup>2</sup> <https://heasarc.gsfc.nasa.gov/docs/software/heasoft/>

<sup>3</sup> <http://cxc.harvard.edu/ciao/>

in the best source position with  $20''$  radius. The background is estimated from an annular region in the same position with radii from  $30''$  to  $60''$ . The *ancillary response files (arfs)* are extracted with *xrtmkarf*. The PC *redistribution matrix file (rmf) version (v.12)* is used in the spectral fits.

The spectral analysis is performed with *XSPEC(v12.10.1)*<sup>4</sup>. We applied the absorption model (*tbabs* in *XSPEC*) to account for interstellar effect due to hydrogen column density (Wilms et al. 2000). Although the Galactic hydrogen column density of the position of PSR J2032+4127 is given as  $(1.2 - 1.5) \times 10^{22} \text{cm}^{-2}$  by Dickey & Lockman (1990); Kalberla et al. (2005), we kept the parameter free while fitting to investigate whether there exists any significant evolution in the absorption parameter during the periastron. We fit the spectrum using the power law model; *tbabs*  $\times$  *po*. The uncertainties are given at 90% confidence levels for one parameter. The joint spectral analysis of *XMM* and *NuSTAR* spectral analysis is done in the 0.5-50 keV energy range. We multiplied the model with a constant parameter to better calibrate different detectors. The constant kept fixed to unity for the *XMM EPIC-PN* spectrum and remained free for *EPIC-MOS1*, *MOS2*, *FPMA*, *FPMB*. On MJD 58062 the 0.5-50 keV joint *XMM+NuSTAR* spectral analysis show the interstellar absorption around  $0.77 \pm 0.06 \times 10^{22} \text{cm}^{-2}$  along with the power-law index  $\Gamma = 1.37 \pm 0.05$  and 0.3-10 keV unabsorbed power-law flux is around  $0.23 \pm 0.004 \times 10^{-11} \text{erg s}^{-1} \text{cm}^{-2}$ . The cross-calibration constant for *FPMA* is obtained as  $1.02 \pm 0.07$  and for *FPMB* is  $0.88 \pm 0.07$  In Fig. 1(a), *XMM+NuSTAR* fitted spectra of MJD 58062 are shown. The *XMM+NuSTAR* spectral analysis results are shown in detail in Table. 2. The cross-calibration constants for different instruments, during the joint *XMM+NuSTAR* spectral analysis with absorbed power-law model, are also reported in Table. 2. Most of the cases the cross-calibration constant values are around unity. For a few cases larger deviations are obtained. May be they are due to the presence of stray light or some other effects (Wik et al. 2014).

The *Chandra ACIS* spectra analyzed with absorbed power-law model within 0.8-10 keV. from the spectral analysis the interstellar absorption is obtained around  $1.06 \pm 0.38 \times 10^{22} \text{cm}^{-2}$  along with the power-law index  $\Gamma = 1.29 \pm 0.28$  and 0.3-10 keV unabsorbed power-law flux is around  $0.29 \pm 0.017 \times 10^{-11} \text{erg s}^{-1} \text{cm}^{-2}$ . The fitted *ACIS* spectrum of MJD 58062 is shown in Fig. 1(b). The *Chandra* spectral analysis results are shown in detail in Table. 3.

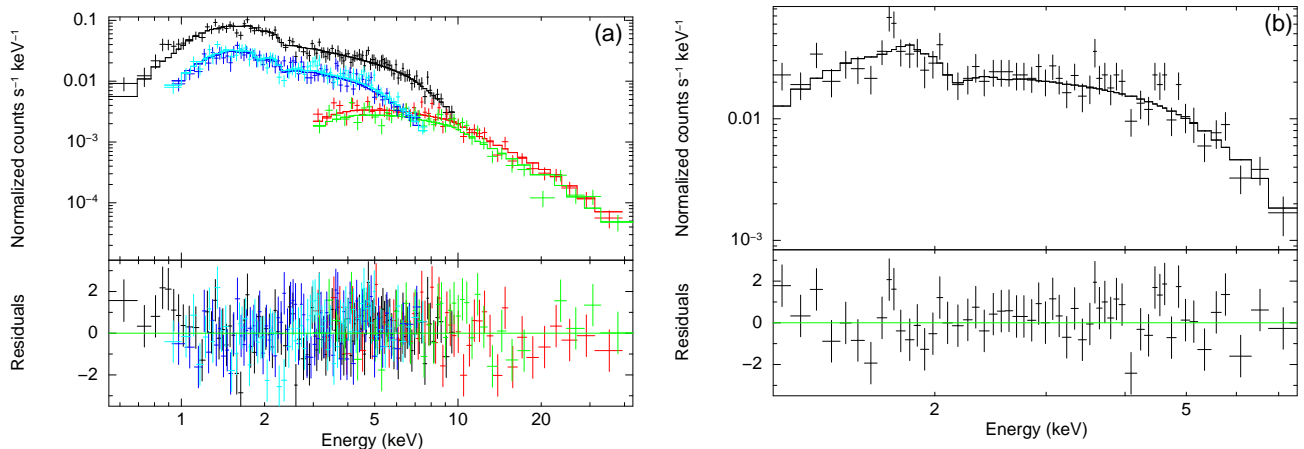


**Figure 1.** (a) Joint *XMM-Newton* and *NuSTAR* absorbed power-law fitted spectra of MJD 58062. The black curve represents *XMM-Newton EPIC-PN* data. Blue and cyan curves represent *XMM-Newton EPIC-MOS1* and *MOS2* data respectively. Red and green curves represent the *NuSTAR FPMA* and *FPMB* data respectively. (b) *Chandra-ACIS* absorbed power-law fitted spectrum of MJD 58062.

From *XMM+NuSTAR* spectral analysis, the average  $n_H$  value is obtained around  $n_H = 0.78 \times 10^{22} \text{cm}^{-2}$ . Here all 1.0-10.0 keV *Swift-XRT* spectra are fitted with the same model component with fixed  $n_H = 0.78 \times 10^{22} \text{cm}^{-2}$ . XRT unabsorbed flux values are shown in Fig. 2 for comparison. In all cases the unabsorbed power-law flux is calculated in 0.3-10 keV energy range in cgs units.

We have calculated the hardness ratio for the X-Ray data. Here hardness ratio is the ratio between 2.0-10.0 keV photons and 0.3-2.0 keV photons.

<sup>4</sup> <https://heasarc.gsfc.nasa.gov/xanadu/xspec/>

**Table 2.** Spectral analysis results for joint observations of *XMM-Newton* and *NuSTAR* with absorbed power-law model. First column shows the observation dates. In second column interstellar absorption values are shown. Third column shows the power-law index. Fourth column shows the 0.3-10 keV unabsorbed flux calculated from analysis results. Fifth column shows the reduced  $\chi^2$  values with degrees of freedom. Next sixth to tenth columns show the cross-calibration constants for different instruments. The cross-calibration constant for *EPIC-PN* is kept fixed to unity during the analysis.

Date	$n_H$	$\Gamma$	Flux	$\chi^2_\nu$	<i>XMM-Newton</i>			<i>NuSTAR</i>	
(MJD)	( $10^{22} \text{ cm}^{-2}$ )		( $10^{-12} \text{ erg s}^{-1} \text{ cm}^{-2}$ )	(dof)	<i>PN</i>	<i>MOS1</i>	<i>MOS2</i>	<i>FPMA</i>	<i>FPMB</i>
58049	$0.85 \pm 0.04$	$1.38 \pm 0.03$	$4.66 \pm 0.05$	1.09(463)	1.0	$0.97 \pm 0.03$	$1.00 \pm 0.03$	$0.96 \pm 0.05$	$0.94 \pm 0.05$
58062	$0.77 \pm 0.06$	$1.37 \pm 0.05$	$2.31 \pm 0.04$	1.13(319)	1.0	$1.02 \pm 0.05$	$1.08 \pm 0.05$	$1.02 \pm 0.07$	$0.88 \pm 0.07$
58070	$0.68 \pm 0.06$	$1.37 \pm 0.06$	$2.00 \pm 0.04$	1.10(238)	1.0	$0.98 \pm 0.06$	$1.05 \pm 0.07$	$0.91 \pm 0.07$	$0.85 \pm 0.07$
58079	$0.78 \pm 0.03$	$1.53 \pm 0.03$	$5.01 \pm 0.06$	1.24(445)	1.0	$1.00 \pm 0.03$	$1.02 \pm 0.03$	$1.00 \pm 0.05$	$0.94 \pm 0.05$
58091	$0.81 \pm 0.05$	$1.63 \pm 0.05$	$3.52 \pm 0.06$	1.04(350)	1.0	$0.98 \pm 0.05$	$1.04 \pm 0.05$	$0.98 \pm 0.06$	$1.04 \pm 0.07$

**Table 3.** Spectral analysis results for *Chandra* observations with absorbed power-law model. First column shows the observation dates. In second column interstellar absorption values are shown. Third column shows the power-law index. Fourth column shows the 0.3-10 keV unabsorbed flux calculated from analysis results. Fifth column shows the reduced  $\chi^2$  values with degrees of freedom.

Date	$n_H$	$\Gamma$	Flux	$\chi^2_\nu$
(MJD)	( $10^{22} \text{ cm}^{-2}$ )		( $10^{-12} \text{ erg s}^{-1} \text{ cm}^{-2}$ )	(dof)
57442	$0.54 \pm 1.27$	$1.93 \pm 1.36$	$0.66 \pm 0.12$	1.75(4)
57785	$1.02 \pm 0.18$	$2.03 \pm 0.18$	$2.04 \pm 0.08$	0.97(91)
57901	$0.97 \pm 0.12$	$1.73 \pm 0.12$	$4.09 \pm 0.11$	0.74(189)
57994	$0.86 \pm 0.13$	$1.45 \pm 0.12$	$3.50 \pm 0.10$	0.89(179)
58060	$0.87 \pm 0.20$	$1.19 \pm 0.16$	$3.28 \pm 0.12$	1.12(119)
58062	$1.06 \pm 0.38$	$1.29 \pm 0.28$	$2.90 \pm 0.17$	1.11(54)
58127	$1.07 \pm 0.12$	$1.68 \pm 0.12$	$3.24 \pm 0.10$	0.90(156)
58193	$0.85 \pm 0.22$	$1.76 \pm 0.24$	$0.95 \pm 0.05$	0.92(59)

For *Swift-UVOT* data reduction, all extensions of sky images are stacked with `uvotimsum`. The source magnitudes are derived with  $3\text{-}\sigma$  significance level from the circular region of  $5''$  radius in the best source position of the stacked sky images from all the filters with `uvotsource`. The background is estimated from an annular region in the same position with radii from  $10''$  to  $20''$ .

During *XMM+NuSTAR* joint observations the correlation between interstellar absorption and power-law index is calculated with 50 steps in both parameters within the error-bar of the parameter. Then 68%, 90% and 99% confidence contours are plotted with red, blue and gray curves in Fig. 3.

During the *XMM+NuSTAR* joint observations we have also performed spectral fit with absorbed broken power-law model. The fitted spectra for MJD 58070 with both absorbed power-law and broken power-law model are plotted in Fig. 4 for comparison.

### 3. RESULTS

We analyze all pre-periastron X-ray data and confirm results published previously. Here we report the results of the spectral analysis of new *Chandra*, *XMM-Newton*, *NuSTAR* and *SWIFT* data. In 7 panel plot of the Fig. 2 we have plotted the analysis result and compared with the TeV analysis results obtained from [Abeysekara et al. \(2018\)](#).

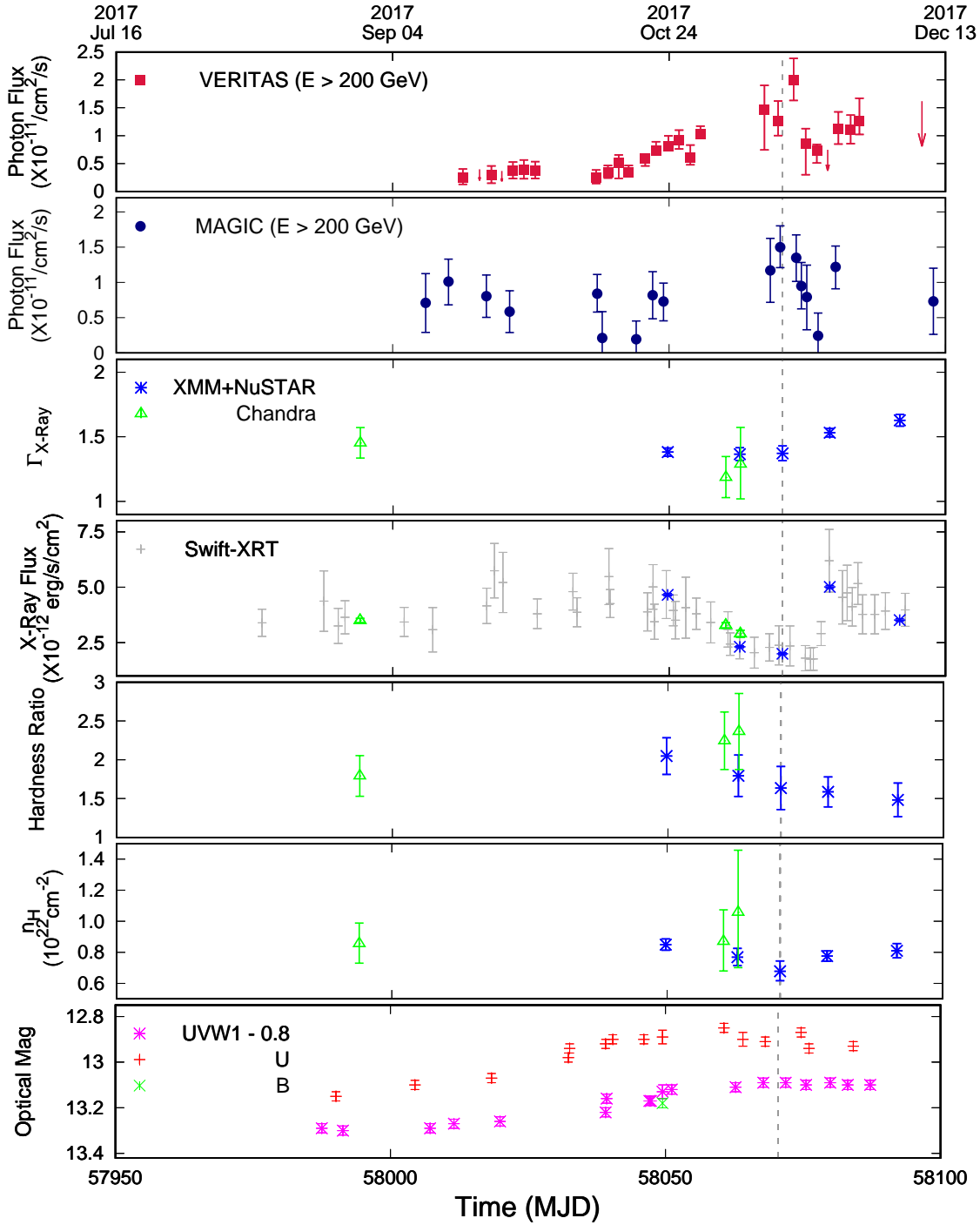


**Figure 2.** Top panel shows the *VERITAS* photon flux light curve. Second panel shows the *MAGIC* photon flux light curve. *VERITAS* and *MAGIC* ( $E > 200$  GeV) data points are obtained from lower panel of Fig. 1(b) of [Abeysekara et al. \(2018\)](#). Third panel shows the variation of X-ray power law index. In the fourth, fifth and sixth panel the Blue stars represent *XMM+NuSTAR* result. Green triangle represents *Chandra* result. Fourth panel shows the 0.3-10 keV unabsorbed power-law flux variation where gray points represent *Swift-XRT* data analysis result. Fifth panel shows the evolution of hardness ratio between 2.0-10.0 keV and 0.3-2.0 keV photons. Sixth panel shows the interstellar absorption obtained from spectral fitting. The bottom panel shows the *UVOT* magnitude in Vega system. Red points represent the U magnitude. Green point represent the B magnitude and pink star represent UVW1 magnitude with offset by 0.8 magnitude. The grey dashed line for all panels represents the periastron on MJD 58070. From third to sixth panel during the X-Ray analysis uncertainties are given at 90% confidence levels.

In the top and second panel of Fig. 2 the TeV photon flux values are reported from *VERITAS* and *MAGIC* observations respectively. These data points are obtained from lower panel Fig. 1(b) of [Abeysekara et al. \(2018\)](#) for comparison. In the top panel the from MJD 58012 to MJD 58042 the *VERITAS* ( $E > 200$  GeV) photon counts are below  $0.5 \times 10^{-11}$  *Counts cm<sup>-2</sup>s<sup>-1</sup>* after MJD 58045 the *VERITAS* counts started increasing gradually to  $1.5 \times 10^{-11}$  *Counts cm<sup>-2</sup>s<sup>-1</sup>* just before the periastron. After the periastron it sharply increase to  $2 \times 10^{-11}$  *Counts cm<sup>-2</sup>s<sup>-1</sup>* and sharply decrease to  $0.75 \times 10^{-11}$  *Counts cm<sup>-2</sup>s<sup>-1</sup>* and then the count rate remain variable around  $1.0 \times 10^{-11}$  *Counts cm<sup>-2</sup>s<sup>-1</sup>*. In the second panel the *MAGIC* ( $E > 200$  GeV) count rates remain varying around  $0.75 \times 10^{-11}$  *Counts cm<sup>-2</sup>s<sup>-1</sup>* during the pre-periastron time span. On periastron the count rate is on its peak at  $1.5 \times 10^{-11}$  *Counts cm<sup>-2</sup>s<sup>-1</sup>*. Then it decreases to  $0.25 \times 10^{-11}$  *Counts cm<sup>-2</sup>s<sup>-1</sup>* within 7 days after the periastron. In the third panel the X-ray power-law index is reported. The *XMM+NuSTAR* power-law index remain steady around  $1.38 \pm 0.03$  from MJD 58049 to MJD 58070, the periastron. Then the spectrum gets softer gradually from  $1.37 \pm 0.03$  to  $1.63 \pm 0.05$  up to MJD 58091. This is shown with blue stars in the plot. The *Chandra* analysis results are also shown in the plot with green triangles for comparison. In the fourth panel the 0.3-10 keV unabsorbed X-ray power-law flux evolution with time is shown. The *XMM+NuSTAR* flux is shown with blue stars. *Chandra* flux is reported with Green triangles. The grey points represent the *Swift-XRT* flux values. From MJD 58050 to 58069 the flux decreases from  $(4.66 \pm 0.05) \times 10^{-12}$  *erg s<sup>-1</sup>cm<sup>-2</sup>* to  $(2.0 \pm 0.04) \times 10^{-12}$  *erg s<sup>-1</sup>cm<sup>-2</sup>* upto its periastron then it increases to  $(5.01 \pm 0.06) \times 10^{-12}$  *erg s<sup>-1</sup>cm<sup>-2</sup>* then decreases to  $(3.52 \pm 0.06) \times 10^{-12}$  *erg s<sup>-1</sup>cm<sup>-2</sup>*, confirming the double-hump structure found previously. We have calculated the hardness ratio between 2.0-10.0 keV photons and 0.3-2.0 keV photons. The fifth panel show the hardness ratio evolution of the X-ray data. The *XMM-PN* data is shown with blue stars which shows a gradual decrease in hardness ratio from  $2.04 \pm 0.24$  to  $1.48 \pm 0.22$ . *Chandra* data is reported with Green triangles. In the sixth panel we show the variation of interstellar absorption variation obtained from fitting. Here we only put *Chandra*(Green triangle) and *XMM+NuSTAR*(Blue star) data. Albeit with large error bars we note that within measurement uncertainties  $n_H$  is consistent with no significant change within 99% confidence level (see Fig. 3) and the best-fit  $n_H$  values are slightly smaller than the Galactic  $n_H$  values ([Dickey & Lockman 1990](#); [Kalberla et al. 2005](#)), but similar to the foreground value estimated by the optical color excess of MT 91-213 (i.e.  $n_H = 0.77 \times 10^{22}$ cm<sup>-2</sup>) ([Camilo et al. 2009](#); [Li et al. 2017b](#)). In the bottom panel we have shown the *UVOT* variation during the periastron. Here we can see a U band magnitude remained constant around 13 magnitude (Vega) and UVW1 filter magnitude remain constant around 14 Mag(Vega). This optical variation is believed to be observed due to optical evolution from the companion star.

In Fig. 3 we show the evolution of the 68%(red), 90%(blue) and 99%(gray) confidence contours between  $n_H$  and  $\Gamma$  obtained from the *XMM+NuSTAR* analysis (assuming power-law).

Any high energy exponential cutoff may represent a signature of an accretion disk around the compact object. We also analyzed the *XMM+NuSTAR* observation with absorbed power-law with exponential cutoff model and we did not observe any presence of cut-off in the observed data. This result confirms that there are no evidence of an accretion disc during periastron, similar to other gamma-ray binaries ([Takahashi et al. 2009](#); [An et al. 2015](#); [Tam et al. 2015](#); [Li et al. 2014](#)).

[Uchiyama et al. \(2009\)](#) has reported, presence of a power-law break around  $5.0 \pm 0.7$  keV for PSR B1259-63 over the periastron passage, as magnetic interaction between shock and pulsar wind. We have tried to fit *XMM+NuSTAR* spectra with absorbed broken power-law model. With broken power-law model we have obtained similar goodness of fit as power-law model for all five epochs. Here we also found a break in power-law, by  $\Delta\Gamma \sim 0.35$  around  $\varepsilon_{br} \sim 5$  keV, during pre-periastron period and increases to  $\varepsilon_{br} = 12.9 \pm 3.9$  keV by  $\Delta\Gamma \simeq 0.7$  exactly at the periastron passage (see Fig. 4). May be this is due to some magnetic properties of wind. The relation between break energy and magnetization parameter of wind for PSR B1259-63 is given by:

$$\varepsilon_{br} \simeq 4 \left( \frac{B}{1.8 G} \right) \left( \frac{\gamma_1}{4 \times 10^5} \right)^2 \text{ keV} \quad (1)$$

(Eq. 9; [Uchiyama et al. 2009](#)). If we assume PSR J2032+4127 and PSR B1259-63 are similar sources and Lorentz factor( $\gamma_1 \sim 4 \times 10^5$ ) for pulsar wind then during periastron passage,  $12.9 \pm 3.9$  keV break energy will represent pulsar wind magnetic field around  $5.8 \pm 1.7$  G for PSR J2032+4127. Interestingly, we found no  $n_H$  change at all in the broken power-law model. Finally, we note that no short-term evolution is observed within each *XMM-Newton*, *NuSTAR* and *Chandra* observation, indicating that the spectral changes happen in longer time scales.

#### 4. DISCUSSION & CONCLUSION

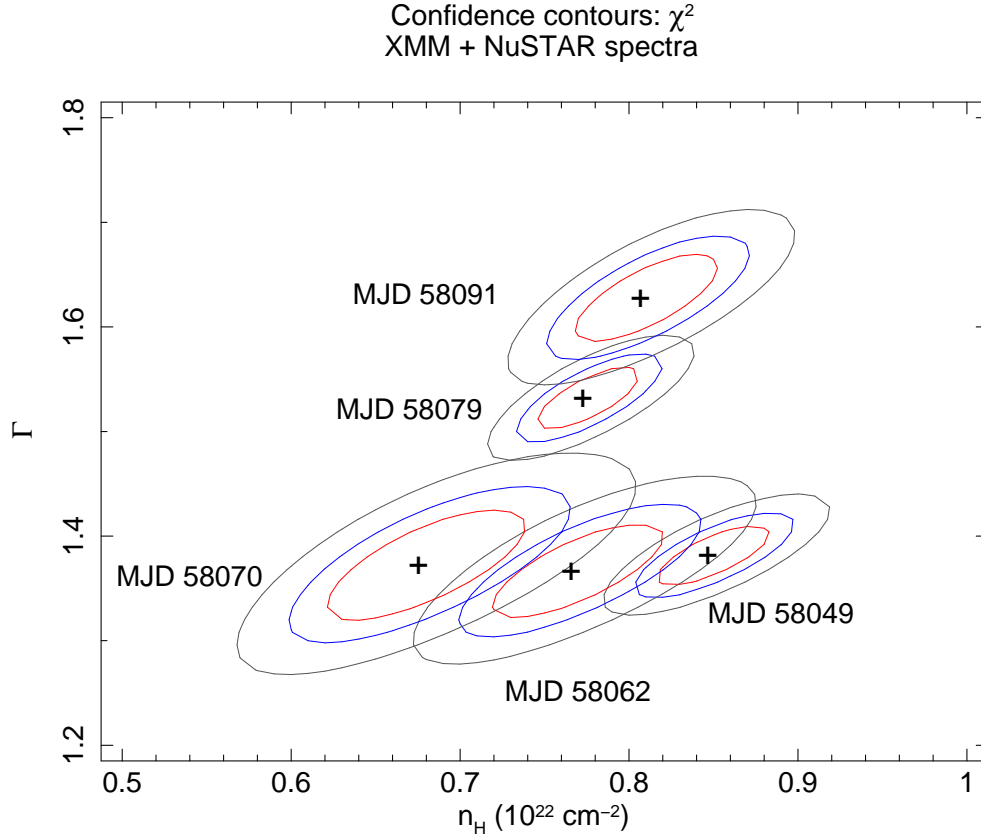


**Figure 3.** Evolution of  $\chi^2$  confidence contours between interstellar absorption and power-law index obtained from *XMM* and *NuSTAR* spectral analysis with power-law model. Here 68% 90% and 99% confidence contours are represented with red, blue and gray curves respectively.

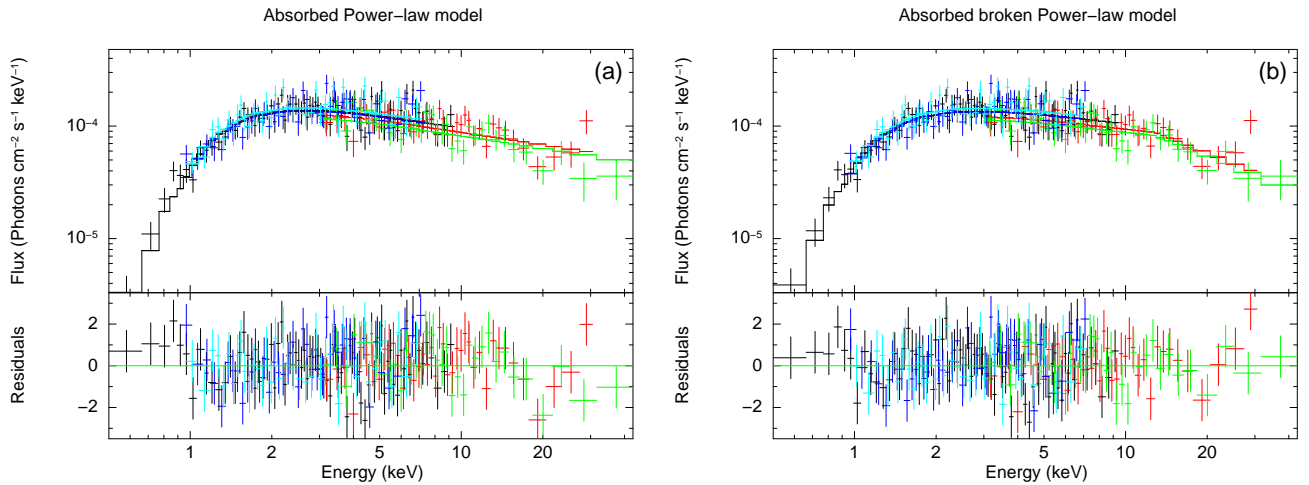


**Figure 4.** (a) Joint *XMM-Newton* and *NuSTAR* absorbed power-law fitted spectra of MJD 58070. (b) Joint *XMM-Newton* and *NuSTAR* absorbed broken power-law fitted spectra of MJD 58070. The black curve represents *XMM-Newton* EPIC-PN data. Blue and cyan curves represent *XMM-Newton* EPIC-MOS1 and MOS2 data respectively. Red and green curves represent the *NuSTAR* FPMA and FPMB data respectively.

The X-ray flux derived from the more accurate X-ray measurements presented in this work is in excellent agreement with those obtained based on *Swift-XRT* only, which has more coverage in time albeit with large errors (Ho et al. 2017; Li et al. 2017b, 2018; Petropoulou et al. 2018). A model light curve developed by Takata et al. (2017) and Li et al.

(2018) generally matches the *Swift-XRT* light curve reasonably well, including the pre-periastron X-ray peak at MJD 58020, and the abrupt drop just before the periastron. As discussed in Li et al. (2018), it is not obvious how the flare-like X-ray emission observed around MJD 58080-58100 is created in the wind-wind interaction model. Furthermore, with the detailed X-ray spectral analysis, we could deliver the evolution of the intrinsic X-ray PL index. Instead, the pulsar wind and Be stellar disk interaction may enhance the X-ray flux, if (1) the scale height of the Be stellar disk at the pulsar position is larger than the shock radius, such that the disk can confine most of the pulsar wind, enhancing the pulsar wind dissipation, and (2) a relatively large base density of the Be stellar disk (Li et al. 2018). One of our major results, namely, a softer intrinsic spectral index (around 1.6) at the post-periastron flare time as compared to that during and before periastron (around 1.4), is in line with a possible new emission region/mechanism at the flare time. The emission mechanism of X-ray photons are driven by Synchrotron emission for binary systems without stellar disc i.e. LS 5039 and 1FGL J1018.6-5856 (Takahashi et al. 2009; An et al. 2015). We note that for PSR B1259-63/LS 2883 system, a softer X-ray power-law index is clearly seen and is thought to be related to the disc passage. Inverse Compton scattering is responsible for the emission of X-ray photons in this system (Chen et al. 2019). Coe et al. (2019) has reported the presence of circumstellar disk and the interaction of the compact object with the circumstellar disk for PSR J2032+4127 during the periastron. Now we can infer that the Inverse Compton Scattering may be the cause of the spectral softening for PSR J2032+4127 after periastron passage.

The Power-law index has shown a clear softening after the periastron, which may indicate the variation in physical state of the shock-accelerated electrons. The fit with broken power-law model also gives similar goodness of fit as we have obtained from power-law model. The increase in break energy from around 5 keV before periastron to around 13 keV at periastron may indicate some physical change during the periastron passage. We do not know the exact cause of the possible changing column density, it can be due to the stellar disk or other components of the stellar winds.

PSP, YC acknowledges sysu-postdoctoral fellowship. PSP, PHT, and YC are supported by NSFC through grants 11633007, 11661161010, and U1731136. We acknowledge the referee for advice to improve the manuscript.

*Facilities:* XMM-Newton, Swift(XRT and UVOT), CXO, NuSTAR

*Software:* HEASOFT(v6.25; [Heasarc](#)), XSPEC(v12.10.1; [Arnaud1996](#)), CIAO(v4.9; [Fruscione et al.2006](#)), SAS(v16.1; [Gabriel et al.2004](#))

## REFERENCES

- Abdo, A. A., Ackermann, M., Ajello, M., et al. 2009, *Science*, 325, 848, doi: [10.1126/science.1176113](#)
- Abdo, A. A., Ajello, M., Allafort, A., et al. 2013, *ApJS*, 208, 17, doi: [10.1088/0067-0049/208/2/17](#)
- Abeysekara, A. U., Benbow, W., Bird, R., et al. 2018, *ApJL*, 867, L19, doi: [10.3847/2041-8213/aae70e](#)
- An, H., Bellm, E., Bhalerao, V., et al. 2015, *ApJ*, 806, 166, doi: [10.1088/0004-637X/806/2/166](#)
- Arnaud, K. A. 1996, in *Astronomical Society of the Pacific Conference Series*, Vol. 101, *Astronomical Data Analysis Software and Systems V*, ed. G. H. Jacoby & J. Barnes, 17
- Bednarek, W., Banasiński, P., & Sitarek, J. 2018, *Journal of Physics G Nuclear Physics*, 45, 015201, doi: [10.1088/1361-6471/aa97ee](#)
- Bogovalov, S. V., Khangulyan, D. V., Koldoba, A. V., Ustyugova, G. V., & Aharonian, F. A. 2008, *MNRAS*, 387, 63, doi: [10.1111/j.1365-2966.2008.13226.x](#)
- Burrows, D. N., Hill, J. E., Nousek, J. A., et al. 2005, *SSRv*, 120, 165, doi: [10.1007/s11214-005-5097-2](#)
- Caliandro, G. A., Cheung, C. C., Li, J., et al. 2015, *ApJ*, 811, 68, doi: [10.1088/0004-637X/811/1/68](#)
- Camilo, F., Ray, P. S., Ransom, S. M., et al. 2009, *ApJ*, 705, 1, doi: [10.1088/0004-637X/705/1/1](#)
- Chen, A. M., Takata, J., Yi, S. X., Yu, Y. W., & Cheng, K. S. 2019, arXiv e-prints, arXiv:1904.07527. <https://arxiv.org/abs/1904.07527>
- Chernyakova, M., Neronov, A., van Soelen, B., et al. 2015, *MNRAS*, 454, 1358, doi: [10.1093/mnras/stv1988](#)
- Coe, M. J., Steele, I. A., Ho, W. C. G., et al. 2017, *The Astronomer's Telegram*, 10920
- Coe, M. J., Okazaki, A. T., Steele, I. A., et al. 2019, *MNRAS*, 485, 1864, doi: [10.1093/mnras/stz515](#)
- Dickey, J. M., & Lockman, F. J. 1990, *ARA&A*, 28, 215, doi: [10.1146/annurev.aa.28.090190.001243](#)
- Dubus, G. 2006, *A&A*, 451, 9, doi: [10.1051/0004-6361:20054233](#)

- Dubus, G., Cerutti, B., & Henri, G. 2010, *A&A*, 516, A18, doi: [10.1051/0004-6361/201014023](https://doi.org/10.1051/0004-6361/201014023)
- Fruscione, A., McDowell, J. C., Allen, G. E., et al. 2006, in *Society of Photo-Optical Instrumentation Engineers (SPIE) Conference Series*, Vol. 6270, Proc. SPIE, 62701V
- Gabriel, C., Denby, M., Fyfe, D. J., et al. 2004, in *Astronomical Society of the Pacific Conference Series*, Vol. 314, *Astronomical Data Analysis Software and Systems (ADASS) XIII*, ed. F. Ochsenbein, M. G. Allen, & D. Egret, 759
- Gaia Collaboration. 2018, *VizieR Online Data Catalog*, 1345
- Harrison, F. A., Craig, W. W., Christensen, F. E., et al. 2013, *ApJ*, 770, 103, doi: [10.1088/0004-637X/770/2/103](https://doi.org/10.1088/0004-637X/770/2/103)
- (Heasarc), N. H. E. A. S. A. R. C. 2014, *HEASoft: Unified Release of FTOOLS and XANADU*. <http://ascl.net/1408.004>
- Ho, W. C. G., Ng, C.-Y., Lyne, A. G., et al. 2017, *MNRAS*, 464, 1211, doi: [10.1093/mnras/stw2420](https://doi.org/10.1093/mnras/stw2420)
- Johnson, T. J., Wood, K. S., Kerr, M., et al. 2018, *ApJ*, 863, 27, doi: [10.3847/1538-4357/aad185](https://doi.org/10.3847/1538-4357/aad185)
- Kalberla, P. M. W., Burton, W. B., Hartmann, D., et al. 2005, *A&A*, 440, 775, doi: [10.1051/0004-6361:20041864](https://doi.org/10.1051/0004-6361:20041864)
- Khangulyan, D., Aharonian, F. A., Bogovalov, S. V., & Ribó, M. 2011, *ApJ*, 742, 98, doi: [10.1088/0004-637X/742/2/98](https://doi.org/10.1088/0004-637X/742/2/98)
- . 2012, *ApJL*, 752, L17, doi: [10.1088/2041-8205/752/1/L17](https://doi.org/10.1088/2041-8205/752/1/L17)
- Kirk, J. G., Ball, L., & Skjæraasen, O. 1999, *Astroparticle Physics*, 10, 31, doi: [10.1016/S0927-6505\(98\)00041-3](https://doi.org/10.1016/S0927-6505(98)00041-3)
- Kolka, I., Eenmäe, T., Laur, J., & Aret, A. 2017, *Research Notes of the American Astronomical Society*, 1, 37, doi: [10.3847/2515-5172/aa9f17](https://doi.org/10.3847/2515-5172/aa9f17)
- Li, J., Torres, D. F., & Zhang, S. 2014, *ApJL*, 785, L19, doi: [10.1088/2041-8205/785/1/L19](https://doi.org/10.1088/2041-8205/785/1/L19)
- Li, K. L., Kong, A. K. H., Tam, P. H. T., et al. 2017a, *ApJ*, 843, 85, doi: [10.3847/1538-4357/aa784e](https://doi.org/10.3847/1538-4357/aa784e)
- Li, K. L., Takata, J., Ng, C. W., et al. 2018, *ApJ*, 857, 123, doi: [10.3847/1538-4357/aab848](https://doi.org/10.3847/1538-4357/aab848)
- Li, K. L., Kong, A. K. H., Takata, J., et al. 2017b, *The Astronomer's Telegram*, 10993
- Lyne, A. G., Stappers, B. W., Keith, M. J., et al. 2015, *MNRAS*, 451, 581, doi: [10.1093/mnras/stv236](https://doi.org/10.1093/mnras/stv236)
- Petropoulou, M., Vasilopoulos, G., Christie, I. M., Giannios, D., & Coe, M. J. 2018, *MNRAS*, 474, L22, doi: [10.1093/mnras/slx185](https://doi.org/10.1093/mnras/slx185)
- Strüder, L., Briel, U., Dennerl, K., et al. 2001, *A&A*, 365, L18, doi: [10.1051/0004-6361:20000066](https://doi.org/10.1051/0004-6361:20000066)
- Takahashi, T., Kishishita, T., Uchiyama, Y., et al. 2009, *ApJ*, 697, 592, doi: [10.1088/0004-637X/697/1/592](https://doi.org/10.1088/0004-637X/697/1/592)
- Takata, J., Tam, P. H. T., Ng, C. W., et al. 2017, *ApJ*, 836, 241, doi: [10.3847/1538-4357/aa5c80](https://doi.org/10.3847/1538-4357/aa5c80)
- Takata, J., Okazaki, A. T., Nagataki, S., et al. 2012, *ApJ*, 750, 70, doi: [10.1088/0004-637X/750/1/70](https://doi.org/10.1088/0004-637X/750/1/70)
- Tam, P. H. T., He, X.-B., Pal, P. S., & Cui, Y. 2018, *ApJ*, 862, 165, doi: [10.3847/1538-4357/aacf00](https://doi.org/10.3847/1538-4357/aacf00)
- Tam, P. H. T., Li, K. L., Takata, J., et al. 2015, *ApJL*, 798, L26, doi: [10.1088/2041-8205/798/1/L26](https://doi.org/10.1088/2041-8205/798/1/L26)
- Tavani, M., & Arons, J. 1997, *ApJ*, 477, 439, doi: [10.1086/303676](https://doi.org/10.1086/303676)
- Turner, M. J. L., Abbey, A., Arnaud, M., et al. 2001, *A&A*, 365, L27, doi: [10.1051/0004-6361:20000087](https://doi.org/10.1051/0004-6361:20000087)
- Uchiyama, Y., Tanaka, T., Takahashi, T., Mori, K., & Nakazawa, K. 2009, *ApJ*, 698, 911, doi: [10.1088/0004-637X/698/1/911](https://doi.org/10.1088/0004-637X/698/1/911)
- Weisskopf, M. C., Tananbaum, H. D., Van Speybroeck, L. P., & O'Dell, S. L. 2000, in *Proc. SPIE, Vol. 4012, X-Ray Optics, Instruments, and Missions III*, ed. J. E. Truemper & B. Aschenbach, 2–16
- Wik, D. R., Hornstrup, A., Molendi, S., et al. 2014, *ApJ*, 792, 48, doi: [10.1088/0004-637X/792/1/48](https://doi.org/10.1088/0004-637X/792/1/48)
- Wilms, J., Allen, A., & McCray, R. 2000, *ApJ*, 542, 914, doi: [10.1086/317016](https://doi.org/10.1086/317016)